

Supporting Information

for

Probing Dielectric Properties of Metal-Organic Frameworks: MIL-53(Al) as a Model System for Theoretical Predictions and Experimental Measurements *via* Synchrotron Far- and Mid-InfraRed Spectroscopy

Kirill Titov,¹ Zhixin Zeng,¹ Matthew R. Ryder,¹ Abhijeet K. Chaudhari,¹ Bartolomeo Civalleri,² Chris S. Kelley,³ Mark D. Frogley,³ Gianfelice Cinque,³ and Jin-Chong Tan^{1,}*

¹*Multifunctional Materials and Composites (MMC) Laboratory, Department of Engineering Science, University of Oxford, Parks Road, Oxford, OX1 3PJ (UK).*

²*Department of Chemistry, NIS and INSTM Reference Centre, University of Turin, via Pietro Giuria 7, 10125 Torino, Italy.*

³*Diamond Light Source, Harwell Campus, Chilton, Oxford, OX11 0DE (UK)*

**E-mail: jin-chong.tan@eng.ox.ac.uk*

Table of Contents

1	Reflectance measurements procedures at the Diamond synchrotron	3
2	Issues of dielectric notations.....	4
3	Characterisation of the surface of the pressed pellets.....	6
4	Specular reflection off a MOF pellet: factors at play	9
5	The measured reflectance spectra	10
6	Real part of the complex dielectric function: closer look at experimental data vs DFT simulations.....	11
7	Imaginary part of the complex dielectric function: closer look at experimental data vs DFT simulations	12
8	Complex refractive index	13
9	Further pelletisation study: WAXS results	14
10	Kramers-Kronig transform (KKT) for specular reflectance data at near normal incidence	17
	10.1 Function to batch calculate the complex refractive index and the complex dielectric function for a set of matching experimental spectra in the Far IR (FIR) and the Mid IR (MIR).....	19
	10.2 Function to smoothly join data and interpolate to 0 wavenumber (called within KKTransform_Publish.m)	20
	10.3 Function to calculate the phase shift (called within KKTransform_Publish.m).....	21
	10.4 Function to calculate the complex refractive index (called within KKTransform_Publish.m).....	22
11	Density functional theory (DFT) calculations of frequency-dependent dielectric properties	23
12	References	24

1 Reflectance measurements procedures at the Diamond synchrotron

The specular reflection experiments were conducted at Beamline B22 MIRIAM in the Diamond Light Source synchrotron (Harwell Campus, Oxfordshire). Specular reflection measurements were carried out in a Bruker Vertex 80V FTIR interferometer, equipped with the Pike Technologies VeeMAX II variable angle specular reflectance accessory (Fig.S1).

Synchrotron IR reflectivity spectra were collected on samples of pressed-powder pellets (diameter = 13 mm, thickness ~ 1 mm) prepared under uniaxial compression varied from 0.1-10 ton (see Fig.1c in main manuscript). Specular reflection was obtained at an angle of 30° from the normal to the pellet's surface, where IR spectra were collected with a resolution of 2 cm^{-1} and 512 scans per spectral scan. Vacuum was pumped to better than 10^{-5} bar and maintained at room temperature (21°C). The synchrotron far-IR (FIR) measurements were performed for the spectral range $1000\text{-}0\text{ cm}^{-1}$ while the mid-IR (MIR) for the range $10000\text{-}0\text{ cm}^{-1}$. The background spectra were collected by measuring the reflectance from a mirror once before the FIR measurements and once before the MIR measurements.

The Kramers-Kronig Transform (KKT)¹ routine implemented in OPUS (version 7.2) was applied to the raw spectral data to compute the complex dielectric function and the complex refractive index for the ranges of $620\text{-}40\text{ cm}^{-1}$ in the FIR and $4000\text{-}600\text{ cm}^{-1}$ in the MIR. The spectral range was chosen on the basis of the quality of the collected data thus minimizing artefacts. We were not able to measure reliably below 40 cm^{-1} during this experiment, therefore our results cover the range of $40\text{-}4000\text{ cm}^{-1}$ (~ 2 to 120 THz).

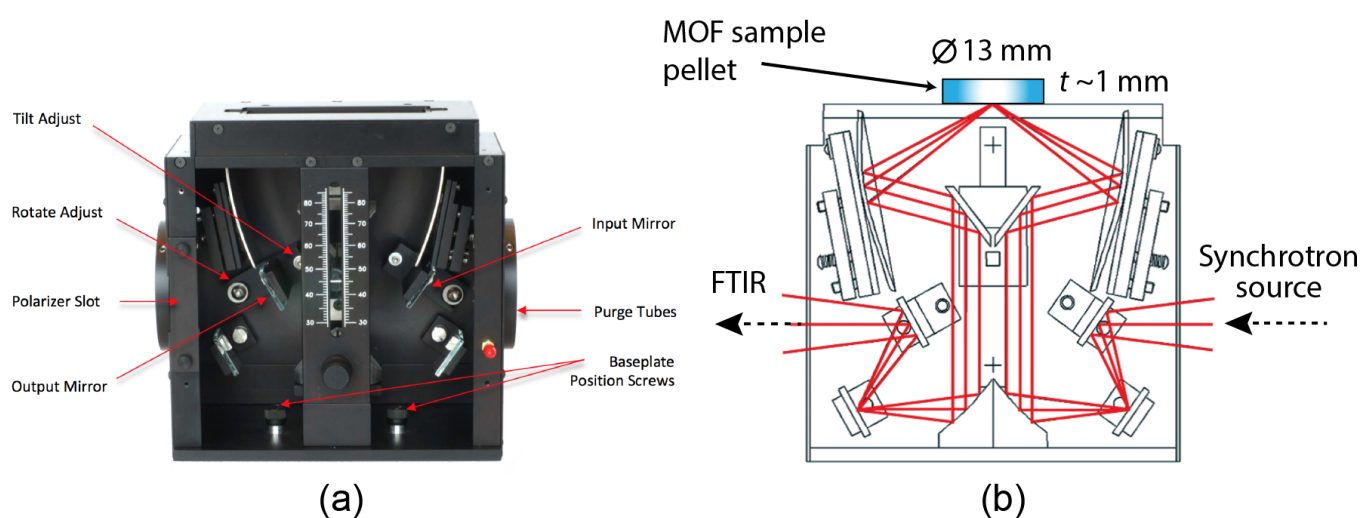


Figure S1. (a) VeeMAX II variable angle specular reflectance accessory, and (b) its optical diagram. Adapted from ref.².

2 Issues of dielectric notations

There is some ambiguity of nomenclature in the literature between the lower frequency dielectric studies, done primarily in the context of capacitor design, and in the optics-related frequency ranges. Herein we set forth the definitions used, in accordance with the standard conventions in the field of optics (based on ‘Optical Properties of Solids’³) as well as in established textbooks on dielectrics (for example, see ref.⁴), and we have further reconciled them with those used by the electronics-oriented literature.

The **complex relative dielectric constant** (or **complex relative permittivity**) as a function of frequency ω is defined as:

$$\tilde{\epsilon}(\omega) = \epsilon'(\omega) + i\epsilon''(\omega)$$

While the **complex refractive index** is defined as:

$$\tilde{n}(\omega) = n(\omega) + i\kappa(\omega)$$

The relationship between the two is:

$$\tilde{n}^2 = \tilde{\epsilon}$$

Combining these into an explicit relationship, we obtain:

$$\epsilon' = n^2 - \kappa^2$$

$$\epsilon'' = 2n\kappa$$

or

$$n = \frac{1}{\sqrt{2}} \left(\epsilon' + (\epsilon'^2 + \epsilon''^2)^{\frac{1}{2}} \right)^{\frac{1}{2}}$$

$$\kappa = \frac{1}{\sqrt{2}} \left(-\epsilon' + (\epsilon'^2 + \epsilon''^2)^{\frac{1}{2}} \right)^{\frac{1}{2}}$$

These expressions describe the propagation of the electric field E due to the incident light wave through a medium with a complex refractive index \tilde{n} :

$$E(z, t) = E_0 e^{i\left(\frac{\omega\tilde{n}z}{c} - \omega t\right)} = E_0 e^{-\frac{\kappa\omega z}{c}} e^{i\left(\frac{\omega n z}{c} - \omega t\right)}$$

where E_0 is the incident electric field, z is the distance into the sample, ω is the frequency of the incident light, t is time and c is the speed of light in vacuum. It is then immediately clear that the imaginary part of the complex refractive index κ leads to losses (i.e. dissipation term).

However, many texts on dielectric behavior (e.g. “Functional Materials vol.2” by Deborah D. L. Chung⁵) simplify their notation and simply define the relative dielectric constant as κ , which varies with frequency, in the context of discussing a parallel plate capacitor with a dielectric between the plates. The loss (imaginary) part of the dielectric constant is taken care of by modeling the capacitor as a system with an ideal capacitor (loss free) and a resistance in parallel. The loss then arises due to a phase difference between the electric displacement field D and the electric field E .

This difference in notation leads to unnecessary ambiguity and confusion. There is merit in consistently using the symbols $\tilde{\epsilon}$ for the complex relative dielectric constant, \tilde{n} for the complex refractive index and the above defined symbols for their real and imaginary parts.

We have demonstrated the application of these self-consistent notations in our manuscript, and do strongly recommend that the increasingly expanding MOF community exploring the ‘new’ field of dielectric properties⁶ adopts this set of consistent notations.

3 Characterisation of the surface of the pressed pellets

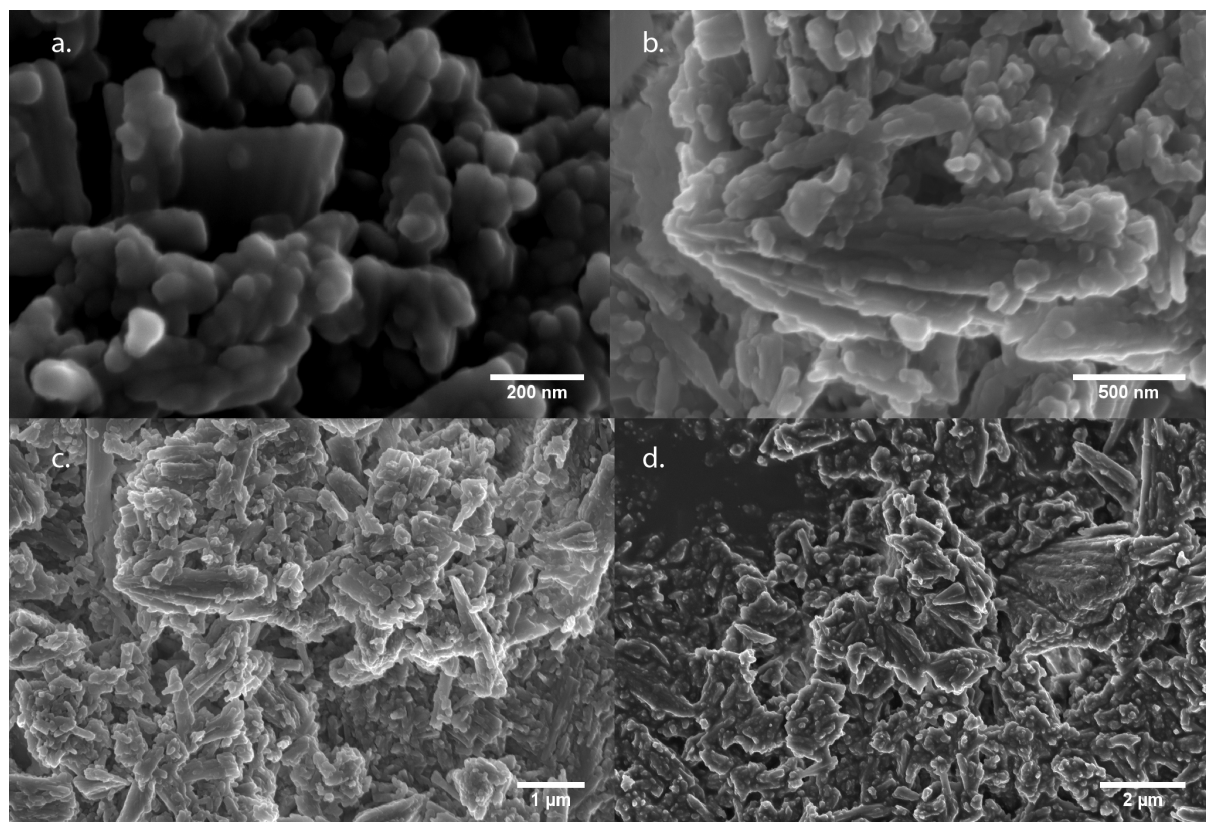


Figure S2. Field Emission Scanning Electron Microscope (FESEM) images of the MIL-53(Al) crystal powder supplied by Sigma Aldrich, showing a size distribution of ~ 50 nm to ~ 2 μm . Images were collected from a carbon-coated powder sample using the InLens detector of a Carl Zeiss Merlin FESEM with EHT of 3 kV and probe current of 100 pA.

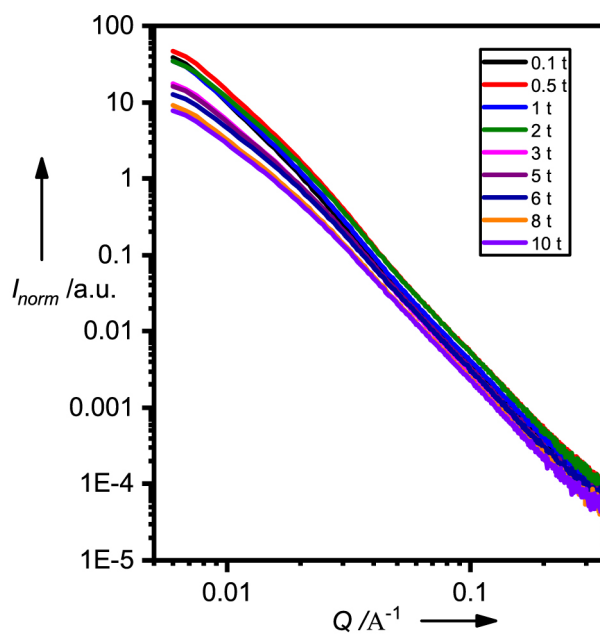


Figure S3. SAXS patterns ($0-4^\circ$) normalized to density*thickness for all pellets.

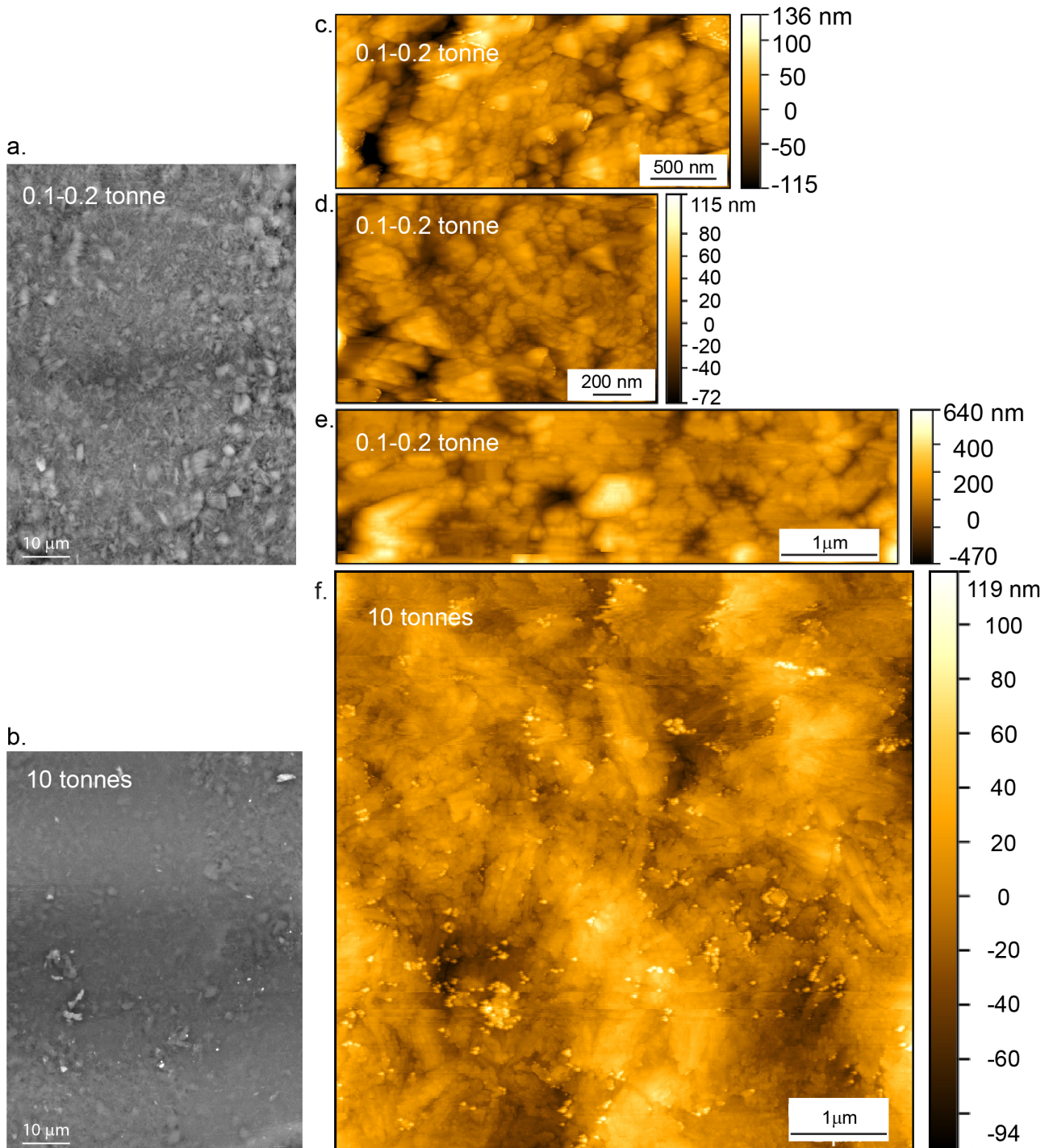


Figure S4. Scanning electron microscopic (SEM) images of MIL-53 pellets moulded under loads (a) 0.1 – 0.2 tonne and (b) 10 tonnes; Atomic force microscopic (AFM) images of MIL-53 pellets moulded under loads (c-e) 0.1 – 0.2 tonne and (f) 10 tonnes. Diameter of the mould is 13mm. AFM images are obtained by the Veeco Dimension 3100 instrument with Tap300Al-G tapping mode AFM probes. Morphological studies of pellets of the highest (10 tonnes) and the lowest (0.1 – 0.2 tonne) loads to evaluate the influence of surface quality of pellets on reflectivity measurement.

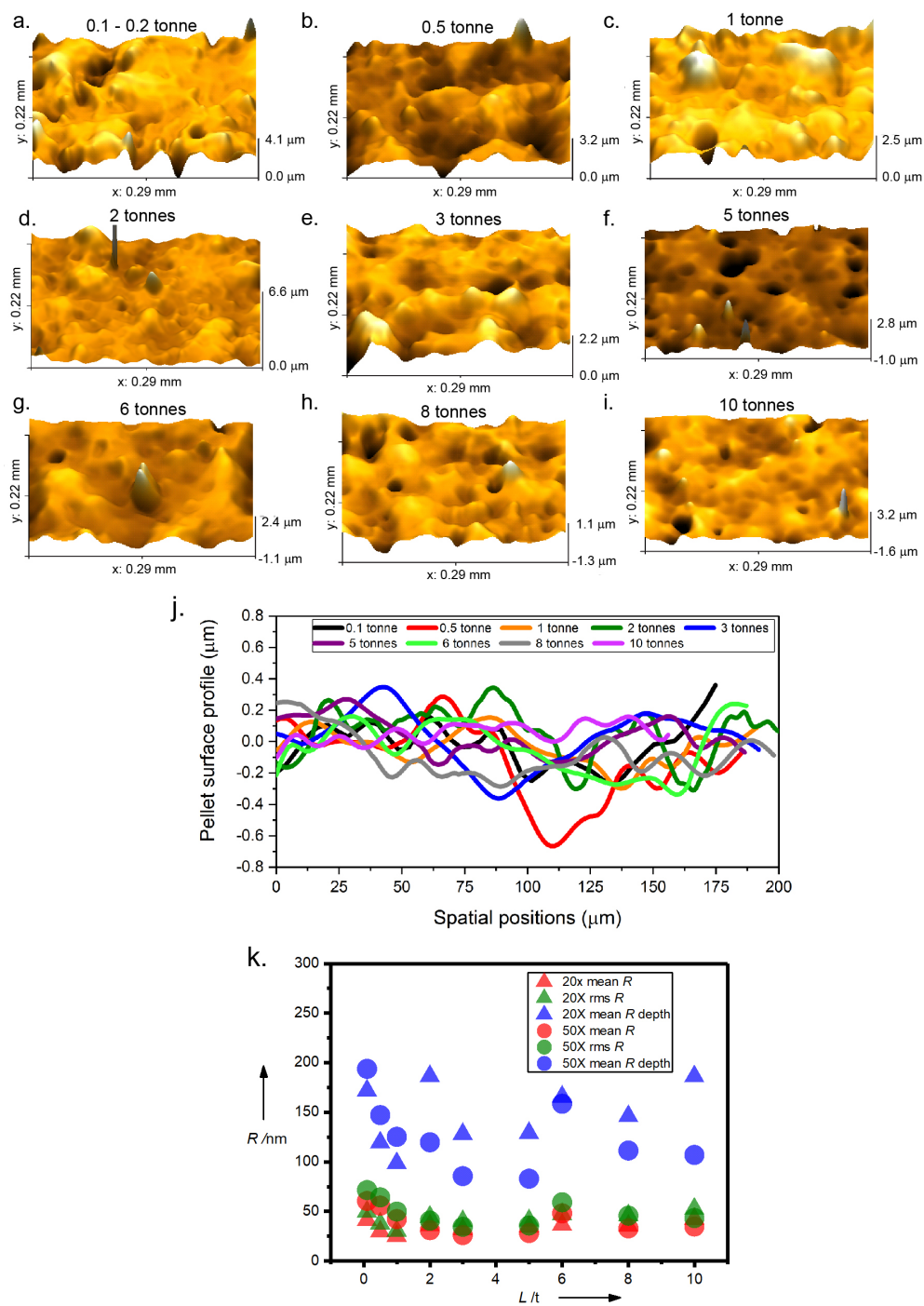


Figure S5. Reconstructed 3D surface profiles (using Alicona InfiniteFocus, 50x objective magnification) of pellets pressed under loads (a) 0.1 – 0.2 tonne, (b) 0.5 tonne, (c) 1 tonne, (d) 3 tonnes, (e) 5 tonnes, (f) 6 tonnes, (g) 8 tonnes, (h) 10 tonnes; (i) Representative cross-sectional profiles of pellets under various loads; (k) three different measures of surface roughness of the pellets at two different magnifications of 20 \times and 50 \times on the Alicona Infinite Focus profilometer. The reconstructed profiles are captured by optical focus-variation technique of Alicona InfiniteFocus instrument, which is equipped with 20 nm vertical resolution (50x objective magnification).

4 Specular reflection off a MOF pellet: factors at play

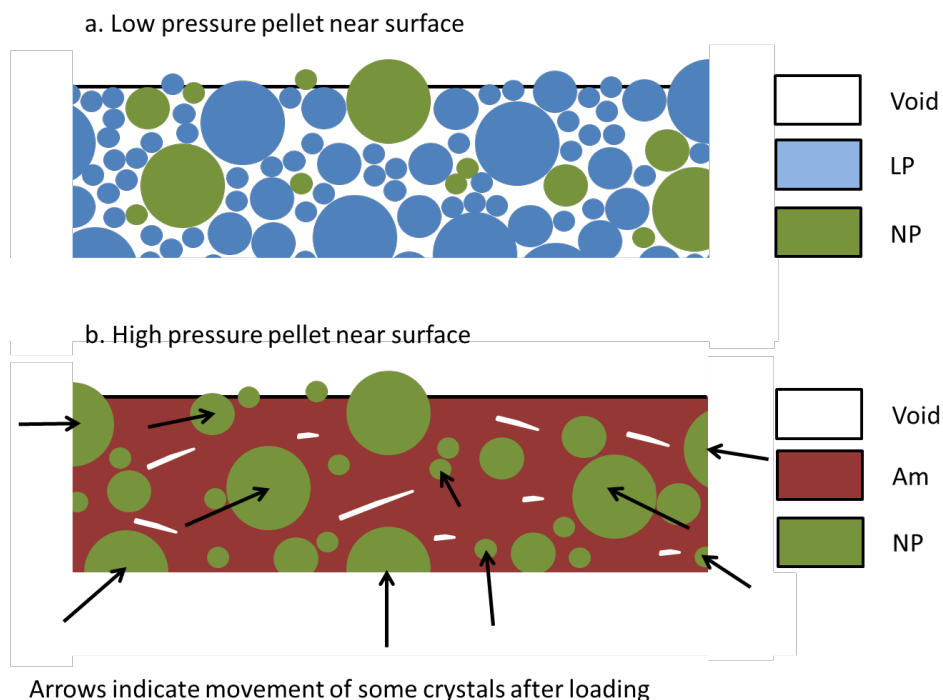


Figure S6. Showing a schematic of the postulated composition of the prepared pellets. The lower pressure pellets (a) consist of LP and NP crystals as well as some voids inbetween due to imperfect packing, while the higher pressure pellets (b) consist of the much better packed amorphised LP crystals (note that these still have porosity, but lack large scale periodicity, hence ‘amorphised’), NP crystals and fewer voids.

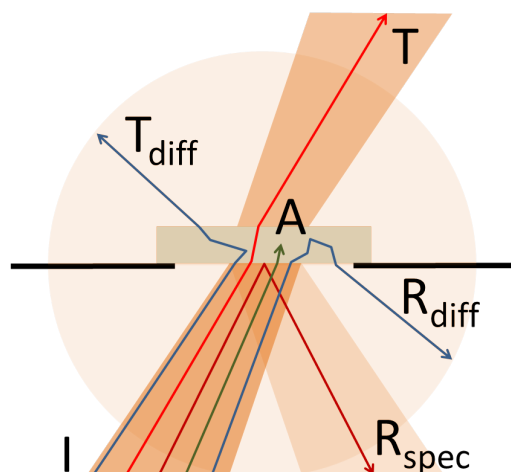


Figure S7. Showing a schematic of the various paths taken by parts of the incident (I) IR beam from the synchrotron source: (A) is absorbed, (T) is transmitted, (T_{diff}) is diffracted and transmitted, (R_{diff}) is diffracted and reflected, and (R_{spec}) is the specular reflected part of the incident beam that was measured in the presented experiments.

5 The measured reflectance spectra

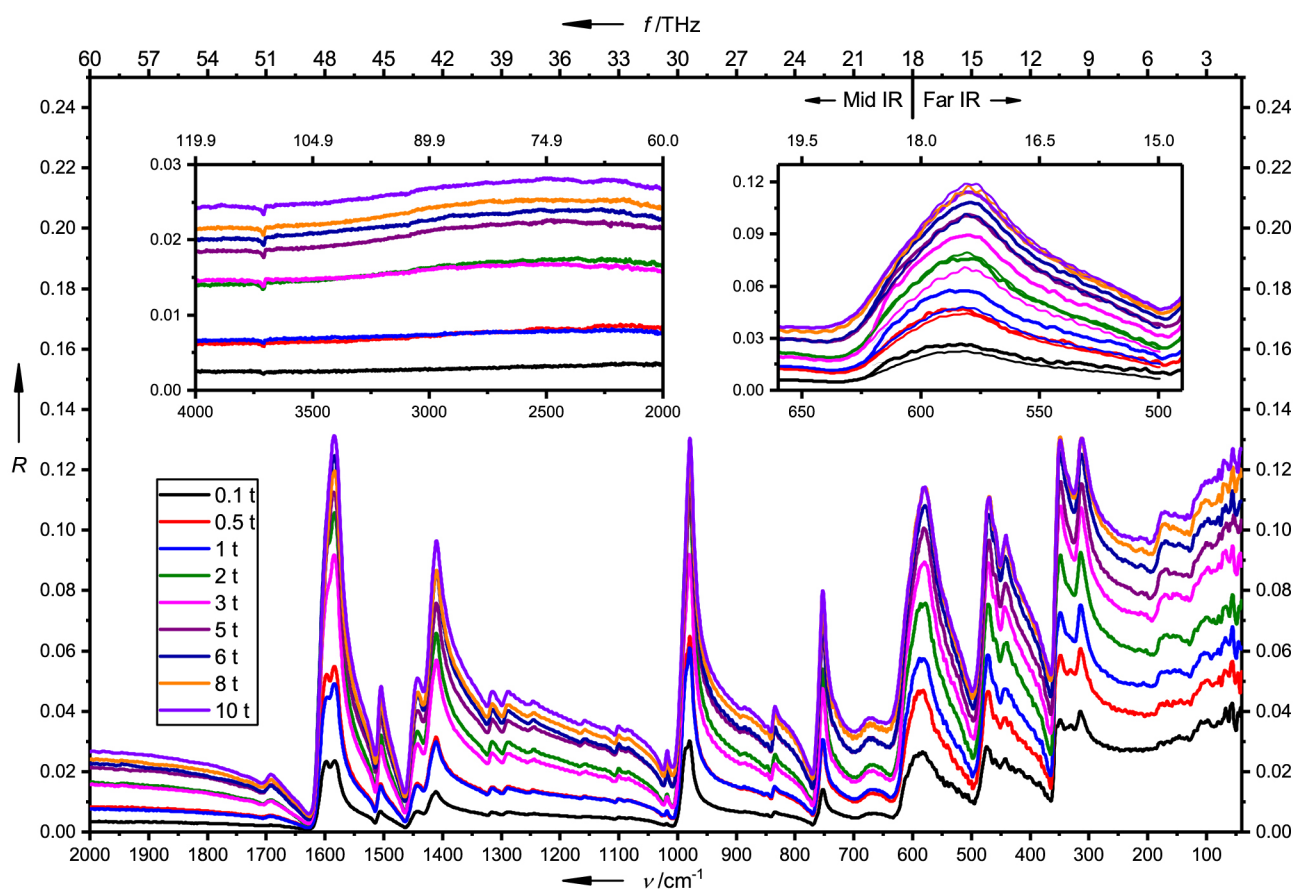


Figure S8. Showing the measured reflectance spectra of MIL-53(Al) pellets. The spectra for the Far IR region have been joined with the Mid IR spectra at 620 cm^{-1} (see section below on details of joining the spectra using Matlab). Inset b) shows the joined curves (thick) with the as measured (thin) Mid IR spectra to demonstrate the good agreement of Far and Mid IR measurements.

6 Real part of the complex dielectric function: closer look at experimental data vs DFT simulations

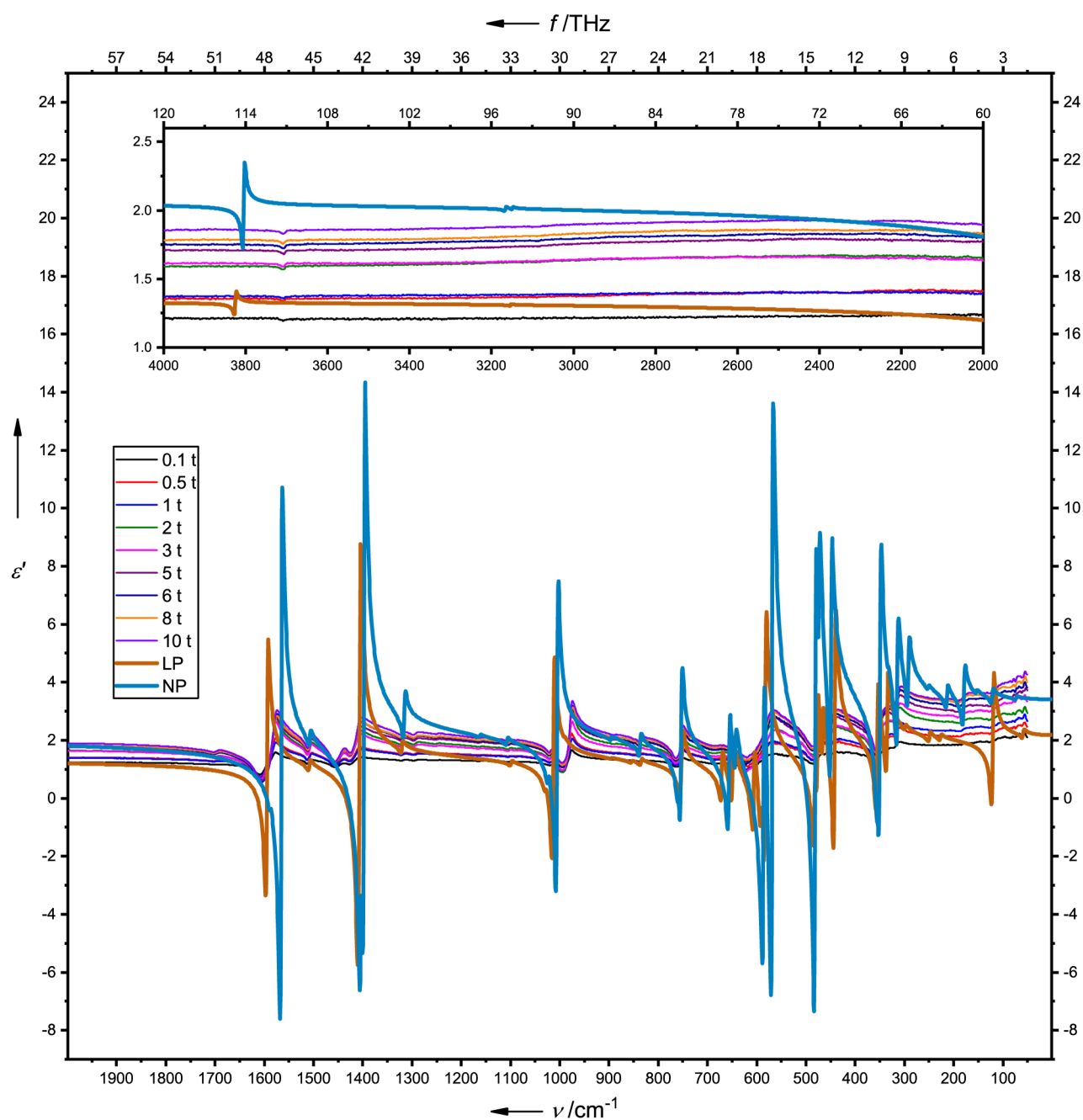


Figure S9. Showing the overlap of the values simulated via DFT versus experimental values. The agreement is superb: all the oscillatory transitions are predicted via DFT and the values rise with increasing NP fraction as predicted via DFT. The inset extends the datasets up to 4000 cm^{-1} .

7 Imaginary part of the complex dielectric function: closer look at experimental data vs DFT simulations

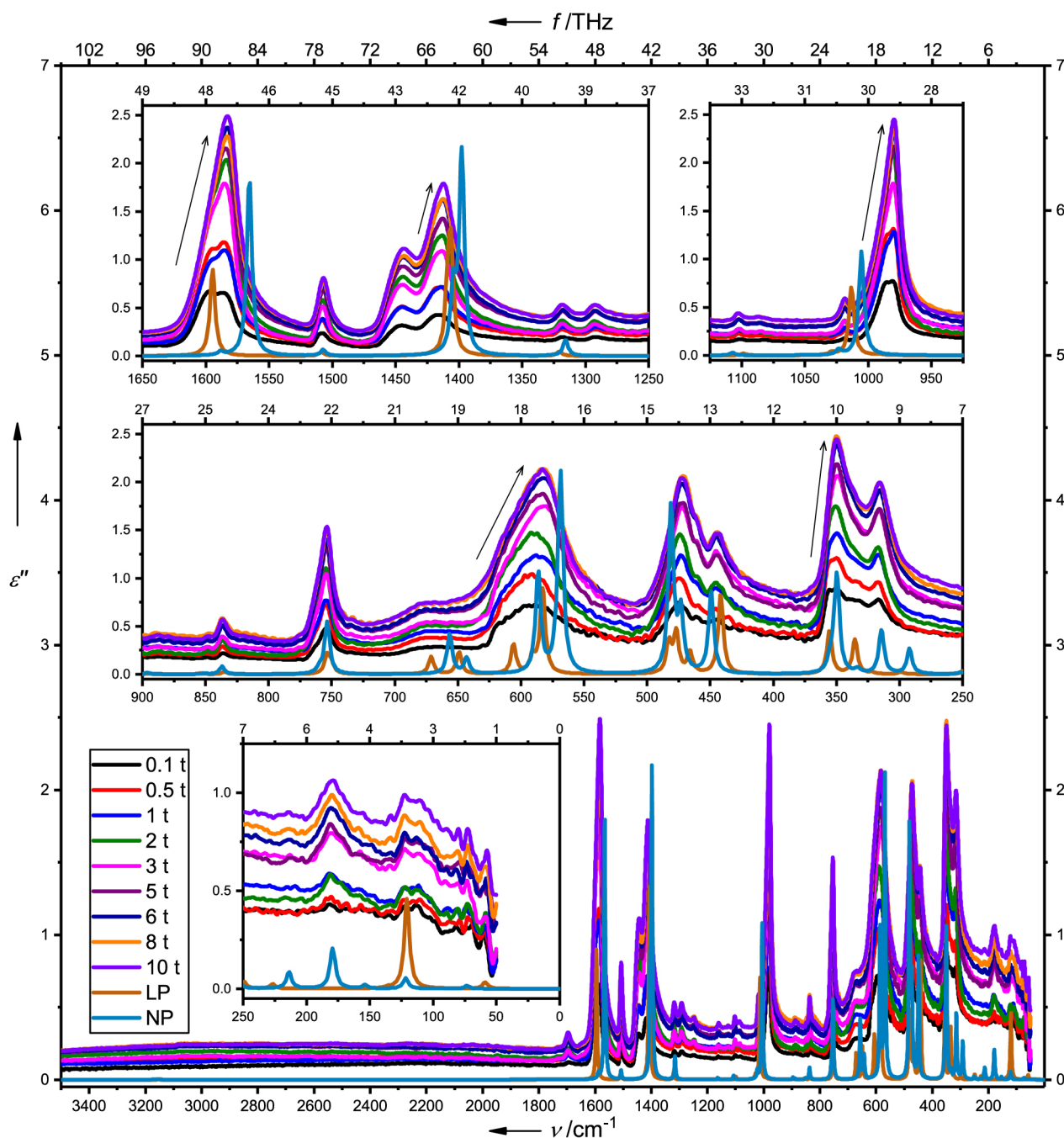


Figure S10. Showing the imaginary part of the complex dielectric function obtained experimentally and via DFT simulation. Insets show a closer view of the various peaks. Importantly, experimental data shows marked shifts and increases in intensity of peaks with decreasing LP content, which are predicted by the DFT simulations of LP versus NP crystals. These shifts are indicated with arrows in the insets. Note that the DFT spectra here are scaled down to be comparable with the experimental data, so it is the positions and the relative intensities of the peaks that are important here, but not the absolute intensities.

8 Complex refractive index

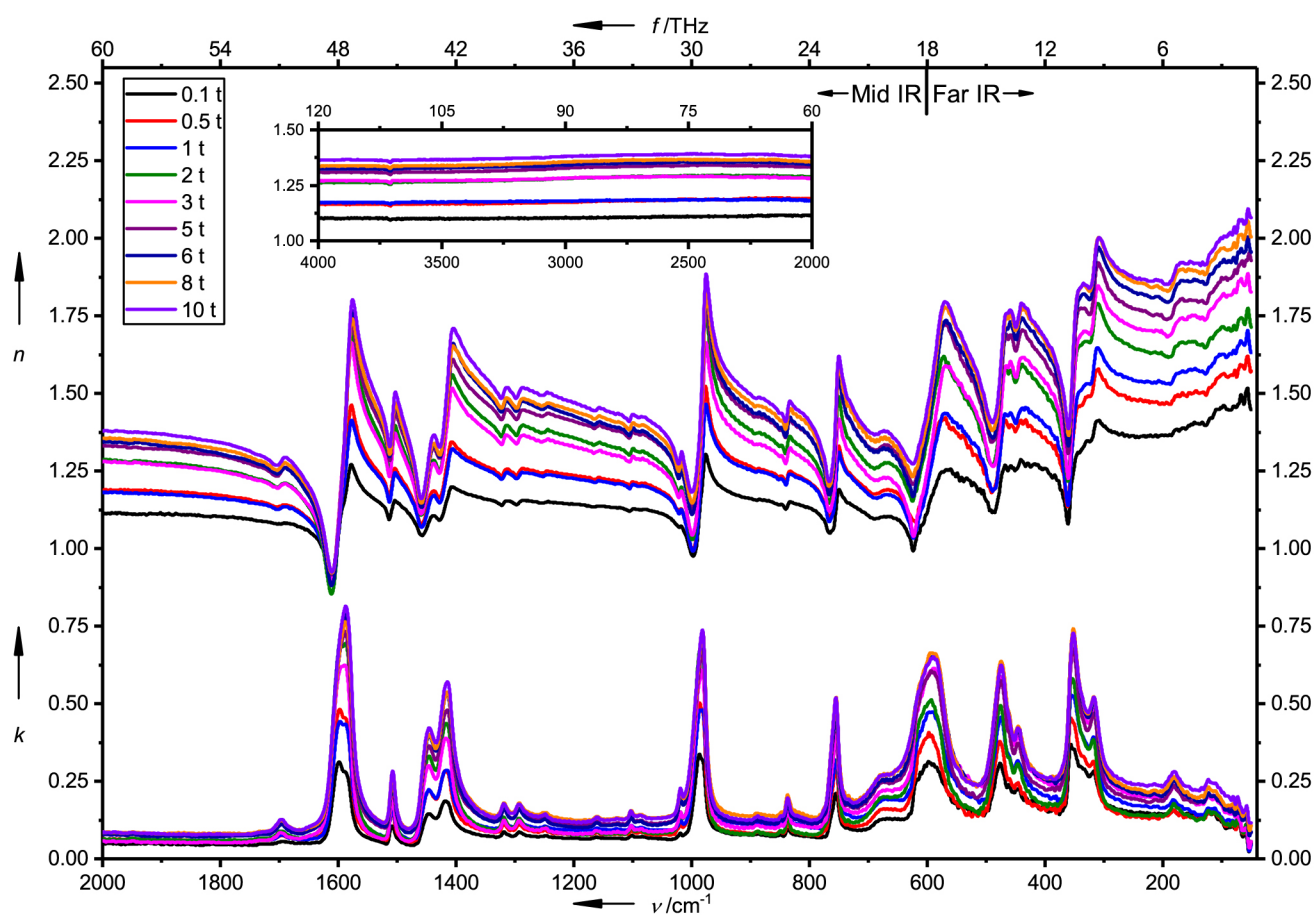


Figure S11. Showing the complex refractive indices of MIL-53(Al) pellets in the form of their real (n) and imaginary (k) parts. The inset shows data for n up to 4000 cm $^{-1}$.

9 Further pelletisation study: WAXS results

The as received MIL-53(Al) powder was subjected to further test to determine its behavior under lab atmosphere conditions and its response to moisture and mechanical stress. As received powder was activated at 315 °C for 20 hr to obtain mostly LP phase powder (obtaining pure LP phase proved to be difficult). Figure S7 shows subsequent powder XRD measurements taken using the MiniFlex machine at increasing times after the activated powder was exposed to the lab's ambient conditions (which are kept relatively dry). The LP content does not appear to dramatically change even after 72 hr of exposure – all the measurements up to this time agree very well. However, as soon as the sample is exposed to water vapor, the XRD pattern changes dramatically (see the 'MintyBreath' patterns in Fig. S7).

This evidence shows that the received MIL-53(Al) LP phase powder is stable under the relevant lab conditions, but converts to NP when water vapor is incident. Thus it is viable to measure a powder sample's XRD pattern, then press a pellet from the same sample and assume that the phase content of the powder remained unchanged up until the time at which stress was applied, so long as no moisture was actively applied to the powder sample.

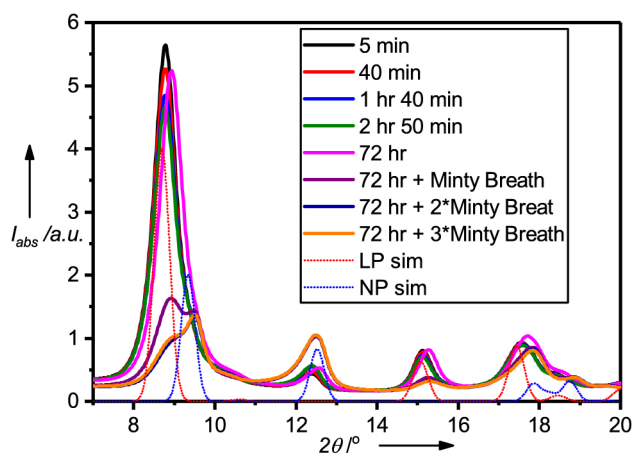


Figure S12. Showing powder XRD patterns measured from the same activated MIL-53(Al) mostly LP powder at increasing times after the powder was exposed to the ISIS R-53 laboratory air (see legend); after 72 hr the powder was exposed to increasing amounts of water vapor.

More powder was activated to further test its response to mechanical stress in the lab pellet press. See Fig. S8-a for powder XRD of the activated powder collected on the MiniFlex instrument. One of the samples was exposed to water vapor so that a portion of crystals converted to NP phase by absorbing water molecules – see pattern 4_MintyBreath compared to the initial pattern 4. These powder samples were then subjected to loads from 0.5 t up to 10 t and the resulting pellets studied using transmission WAXS on the InXider instrument. The results are presented in Fig. S8-b. For clarity of comparison all the data is further plotted in Fig. S7 to juxtapose the starting powder XRD patterns with the patterns

collected from the resulting pellets. It is important to note that the powder XRD curves in Fig. S9 (black and blue curves) were normalised 0 to 1 while the pellet WAXS curves were all normalised by density*thickness of the pellets. Thus only the like-for-like measurements can be compared numerically between themselves: the powder XRD collected using MiniFlex and the pellet WAXS collected using InXider (this is how they are grouped in Fig. S8).

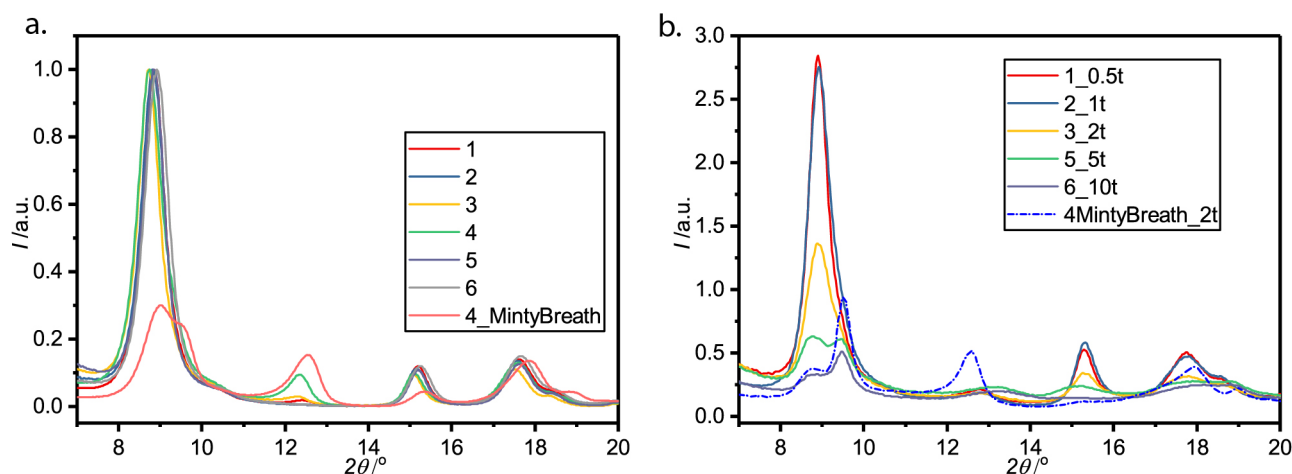


Figure S13. Showing a) the activated MIL-53(Al) powder XRD collected on MiniFlex; b) WAXS patterns of pellets pressed from the activated powder in (a). Legend gives sample numbers and where appropriate the load applied during pelletisation. ‘MintyBreath’ sample was subjected to water vapor before pelletisation.

The most important evidence in all this data lies in the comparison between the pellets pressed from pure LP powders and the pellet pressed from the powder exposed to water vapor. The WAXS patterns show that pressing LP phase powder does not produce anywhere near the same magnitude of NP WAXS peaks (9.8° and 12.5°) compared to magnitudes of those peaks in the pellet made from powder with significant initial NP phase content (the 4_MintyBreath sample). This can be clearly seen in Fig. S8-b, where the 12.5° peak of sample 4MintyBreath_2t is much more intense than any of the other samples; and also in Fig. S9-f where the high NP phase content pellet is compared to the pellet also pressed under 2 t but from purely LP powder. What is also important to note that the LP peaks (8.9° and 15.2°) have drastically diminished in the NP pellet (4MintyBreath_2t) in terms of their relative intensity to the NP peaks compared to the starting powder (4_MintyBreath).

Together the above discussed evidence shows conclusively that subjecting MIL-53(Al) to uniaxial mechanical stress in a closed cylindrical vessel leads to the collapse of LP phase crystals, while only a small fraction of those LP crystals convert to NP phase. At the same time, the NP phase crystals appear to survive the stresses applied in this study, which makes them mechanically more robust compared to their LP counterparts.

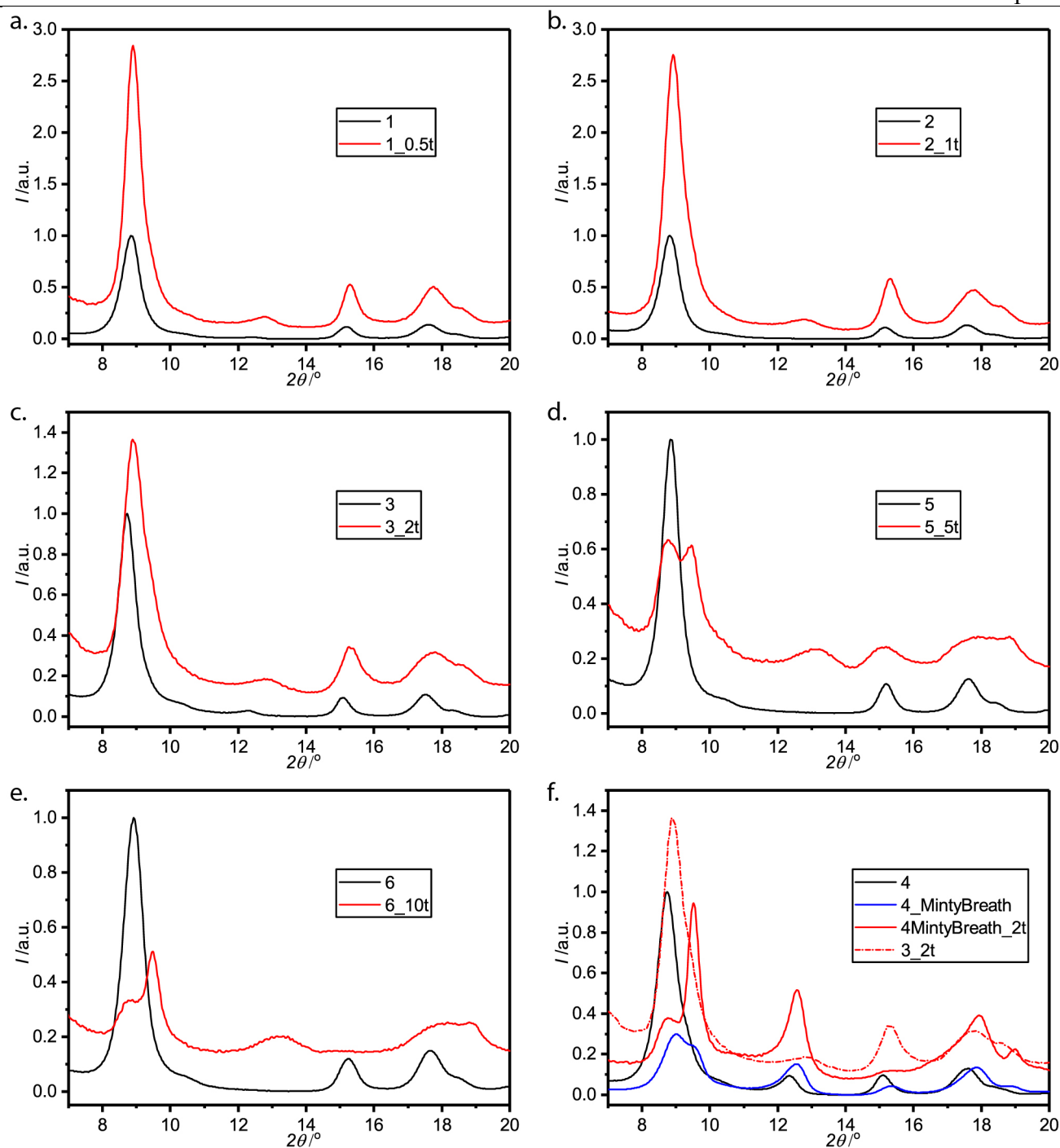


Figure S14. Comparing the (normalized 0 to 1) activated powder XRD with the WAXS pattern of the pellet pressed from that powder. Panel (f) aims to highlight the difference in resulting pellet composition when the starting powder has almost no NP phase (3, see panel c) versus the large starting NP content (4_MintyBreath): the NP content of sample 3_2t is nowhere near that of sample 4MintyBreath_2t (simply comparing the magnitudes of the NP peaks of the two red curves at 9.8°).

10 Kramers-Kronig transform (KKT) for specular reflectance data at near normal incidence

The basis of the transformation used in the present paper are the Kramers-Kronig relations, which are themselves based on the principle of causality of physical systems and connect the real and imaginary parts of many complex quantities in physics ⁷. In particular, the much studied Kramers-Kronig transform between $\frac{1}{2} \ln [R(\nu)/R_\infty]$ and the phase change upon reflection $\varphi(\nu)$ is the key to computing the optical and dielectric properties in this paper. Here R stands for reflectance and ν stands for wavenumber. In the case of external reflection at normal incidence (our experimental conditions are an approximation of these) the following relation holds ⁷:

$$\varphi(\nu_a) = \frac{-2\nu_a}{\pi} P \int_0^\infty \frac{\frac{1}{2} \ln [R(\nu)/R_\infty]}{\nu^2 - \nu_a^2} d\nu$$

where the P designates the Cauchy principle value of the integral. It is important to note here that this integral considers reflectance data from zero to infinity for each individual value of phase change being calculated. From this stem the problems with the Kramers-Kronig transform built into Opus: the transform only takes as input the necessarily limited piecewise measurements (in our case 40-600 cm^{-1} for far IR measurements and 600-4000 cm^{-1} for mid IR measurements). This problem results in physically intractable negative values for the imaginary parts of the complex refractive index and complex dielectric function: the imaginary part is the loss coefficient, and negative loss implies a gain, which is impossible in the absence of a power source (as is the case for a passive material). The following Matlab code solves this problem by smoothly joining the far and mid IR spectra and interpolating to 0 wavenumber to get a single continuous reflectance spectrum, which does a much better job of approximating an infinite dataset. The reflectance is assumed to remain constant from the lowest wavenumber reflectance value measured, while reflectance at infinity R_∞ is assumed to be the highest wavenumber reflectance value measured. Observing that the complex refractive index is given by ⁷:

$$n = \frac{1 - R}{1 + R - 2\sqrt{R} \cos \phi}, k = \frac{-2\sqrt{R} \sin \phi}{1 + R - 2\sqrt{R} \cos \phi}$$

and then using the relation to the complex dielectric function given in section 2 above, the following Matlab code calculates both properties given experimentally measured reflectance spectra. The KKphase function was inspired by the algorithms given as supplementary code with the book "Kramers-Kronig Relations in Optical Materials Research" ¹. To use the code, save the functions in a single .m file with the KKtransform_Publish function on top and call in accordance to instructions contained within the header comments.

Figure S8 compares the output of this code to the output of Opus built in transform to demonstrate the former's advantages over the latter.

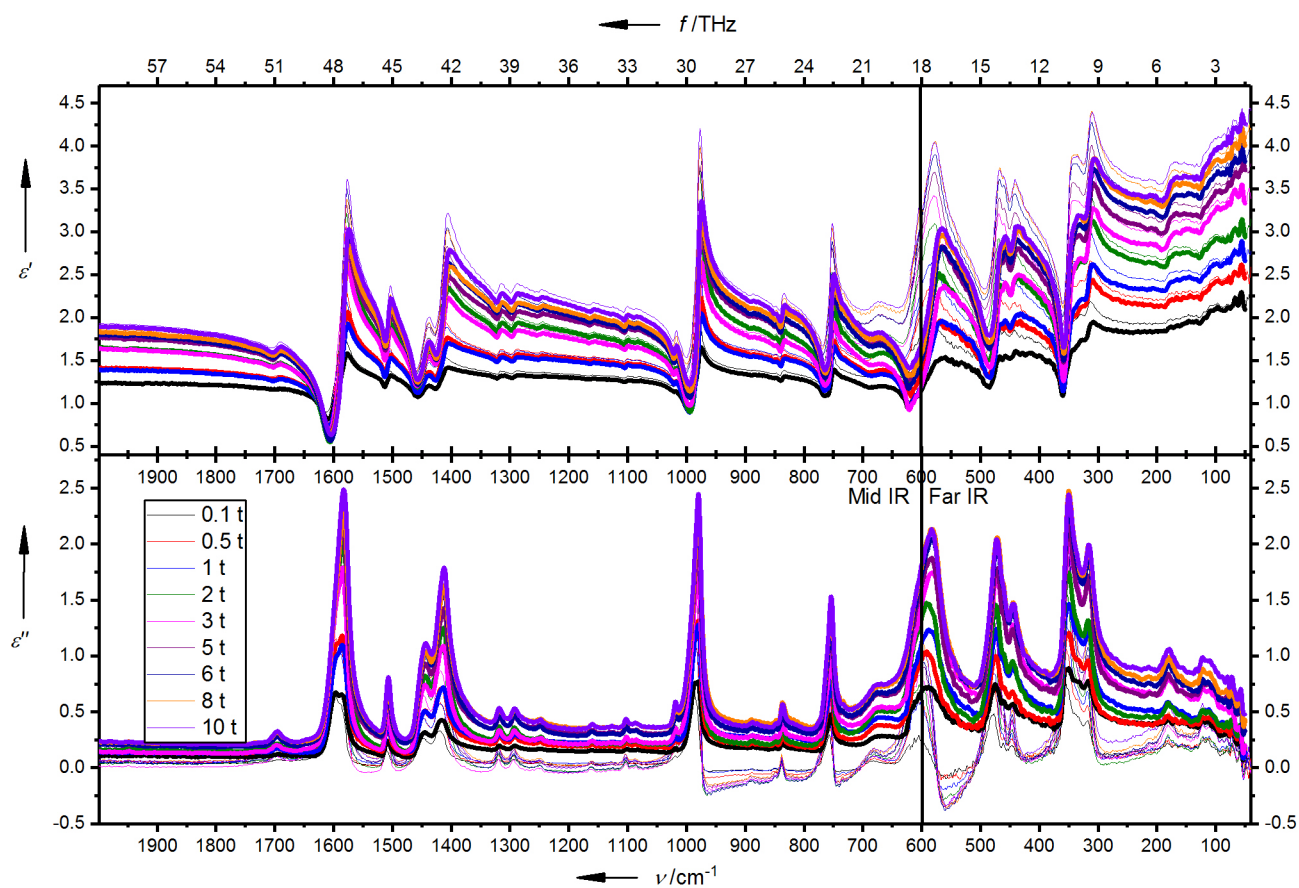


Figure S15. Opus transform output (thin spectra) versus own transform output (thick spectra) of the complex dielectric function. Note the physically intractable negative values in the imaginary part of Opus output and the corresponding higher peaks of the real part.

10.1 Function to batch calculate the complex refractive index and the complex dielectric function for a set of matching experimental spectra in the Far IR (FIR) and the Mid IR (MIR).

```

% Inputs:
% njufar - wavenumber vector in FIR;
% njumid - wavenumber vector in MIR;
% Rfar - reflectance data in FIR;
% Rmid - reflectance data in MIR;
% lowcutindex - index at which to trim data at the low limit of FIR;
% joinnju1 - wavenumber at which to start the joint of FIR and MIR data
% joinnju2 - wavenumber at which to end the joint of FIR and MIR data
% lownjugain - factor increase of reflectance at low wavenumber, this will
% determine the constant straight line extrapolation to low wavenumbers.
% resolution - what resolution is the data? 1cm-1?2cm-1?4cm-1?etc.

% Outputs:
% njunju - the wavenumber vector for the whole range
% RR - the joined reflectance spectra
% n - the real part of the complex refractive index
% k - the imaginary part of the complex refractive index
% epsR - the real part of the complex dielectric function
% epsIm - the imaginary part of the complex dielectric function

function [njunju, RR, n, k, epsR, epsIm] =...
    KKTransform_Publish(njufar, njumid,Rfar, Rmid,...
        lowcutnju, joinnju1, joinnju2, lownjugain, resolution)
% How many pellets? m
[~, m] = size(Rfar);
% Trim the Far IR data at the lower end
i = 1;
while njufar(i) < lowcutnju
    i = i + 1;
end
njufar = njufar(i:end);
Rfar = Rfar(i:end,:);
% Data treatment: join and interpolate data
[RR, njunju] = treatdata(njufar,njumid,Rfar,Rmid,...
    joinnju1,joinnju2,lownjugain, resolution);
% Initialise vectors for refractive index outputs
n = zeros(size(RR));
k = zeros(size(RR));
% Compute the complex refractive index for each pellet
for j = 1:m
    [n(:,j), k(:,j)] = refrInd(njunju, RR(:,j));
end
% Compute the complex dielectric function
epsR = n.^2-k.^2;
epsIm = 2*n.*k;
% Trim the data at the lower end to match the measured range
njunju = njunju(i:end);
RR = RR(i:end,:);
n = n(i:end,:);
k = k(i:end,:);
epsR = epsR(i:end,:);
epsIm = epsIm(i:end,:);
% Plot the complex refractive index and the complex dielectric function
figure(1);

```

```

plot(njunju, n, njunju, k);
xlabel('cm-1');
ylabel('Imaginary (bottom) and Real (top) parts');
title('Complex Refractive Index');
figure(2);
plot(njunju, epsR, njunju,epsIm);
xlabel('cm-1');
ylabel('Imaginary (bottom) and Real (top) parts');
title ('Complex Dielectric Function');
end

```

10.2 Function to smoothly join data and interpolate to 0 wavenumber (called within KKTransform_Publish.m)

```

function [RR, njunju] = treatdata(njuF,njuM,rF,rM,joinnju1,joinnju2,G, res)
% How many pellets? m
[~, m] = size(rF);
% set up the wavenumber vector, which will guide the sampling of the
% pchip algorithm sample at twice the experimental sampling rate
njunju = [0.2:res/2:njuM(end)]';
% set up the output reflectance matrix
RR = zeros(length(njunju),m);
% Determine the joint end index
if joinnju2 > njuM(1)
    i = 1;
    while njuM(i) < joinnju2
        i = i + 1;
    end
    rM = rM(i:end,:);
    njuM = njuM(i:end);
end
% Determine the joint start index
if joinnju1 < njuF(1)
    h = 1;
    while njuF(h)<joinnju1
        h = h+1;
    end
    rF = rF(1:h, :);
    njuF = njuF(1:h);
end
% Treat each pellet's data
for j=1:m
    % Extrapolate the data to 0.5 cm-1
    njuExtra = (0.5:0.5:njuF(1)-5)';
    rExtra = ones(length(njuExtra),1)*rF(1,j)*G;
    % Put the extrapolation, FIR and MIR data into a single vector
    y = [rExtra;rF(:,j);rM(:,j)];
    x = [njuExtra; njuF;njuM];
    % Fit a pchip line to the data, sampling at wavenumbers specified by
    % njunju
    RR(:,j) = pchip(x,y,njunju);
end
% Plot the treated spectra
figure(3);
plot(njunju,RR);
xlabel('cm-1');

```

```
ylabel('Treated Reflectivity');
end
```

10.3 Function to calculate the phase shift (called within KKTransform_Publish.m)

```
function phase = KKphase(nju, R)
% Use the KK-derived relation to calculate the phase shift of the IR signal
g = length(nju);
% Initialise output vector
phase = zeros(length(nju),1);
% Initialise holding vectors
a = zeros(length(nju),1);
b = zeros(length(nju),1);
% What's the wavenumber step?
dnju = nju(3)-nju(2);
% Assume R(infinity) = R(furthest we measured)
Rinf = R(g);
% calculate the first element of the phase shift vector
j = 1;
beta1 = 0;
for k = 2:g
    b(j) = beta1 + (0.5*log(R(k)/Rinf)/(nju(k)^2-nju(j)^2));
    beta1 = b(j);
end
phase(j) = (-2*nju(j)/pi)*b(j)*dnju;
% calculate the last element of the phase shift vector
j = g;
alpha1 = 0;
for k = 1:g-1
    a(j) = alpha1 + (0.5*log(R(k)/Rinf)/(nju(k)^2-nju(j)^2));
    alpha1 = a(j);
end
phase(j) = (-2*nju(j)/pi)*a(j)*dnju;
% loop the inner elements of the phase shift vector
for j = 2:g-1
    alpha1 = 0;
    beta1 = 0;
    for k = 1:j-1
        a(j) = alpha1 + (0.5*log(R(k)/Rinf)/(nju(k)^2-nju(j)^2));
        alpha1 = a(j);
    end
    for k = j+1:g
        b(j) = beta1 + (0.5*log(R(k)/Rinf)/(nju(k)^2-nju(j)^2));
        beta1 = b(j);
    end
    phase(j) = (-2*nju(j)/pi)*(a(j)+b(j))*dnju;
end
end
```

10.4 Function to calculate the complex refractive index (called within KKTransform_Publish.m)

```
function [n, k] = refrInd(nju, R)
n = zeros(length(nju),1);
k = zeros(length(nju),1);

phase = KKphase(nju, R);
for i = 1:length(nju)
    n(i) = (1-R(i))/(1+R(i)-2*(R(i).^0.5).*cos(phase(i)));
    k(i) = (2*(R(i).^0.5).*sin(phase(i)))/(1+R(i)-2*(R(i).^0.5)...
        .*cos(phase(i)));
end
end
```

11 Density functional theory (DFT) calculations of frequency-dependent dielectric properties

Density functional theory (DFT) calculations were performed using a development version of the ab-initio periodic program CRYSTAL14⁸. We have used the B3LYP hybrid exchange-correlation functional augmented with the Grimme's dispersion correction D3 (i.e. B3LYP-D3)⁹ in combination with an Alhrichs' triple-zeta quality (TZP) basis sets.¹⁰ The MIL-53 LP and NP structures have been geometrically optimized in accordance with Ref.¹¹. The vibrational frequency calculations were performed with additional CRYSTAL keywords (listed below), to incorporate the contributions of nuclear motions to the static dielectric constants.

```
FREQCALC
NUMDERIV
2
INTENS
INTCPHF
END
IRSPEC
REFRIND
DIELFUN
DAMPFAC
5.0
GAUSS
ENDIR
END
```

The computed data provide a prediction of the reflectance spectrum and the complex dielectric function at 0 K, for an idealized (defect free) MIL-53 LP/NP structure of well-defined symmetry, namely: orthorhombic (*Imma*) and monoclinic (*C2/c*), respectively. The three values (*x*, *y*, *z*-directions, due to tensorial property) of the real and imaginary parts of the dielectric function were obtained through Kramers-Kronig relations¹², then averaged, and plotted as the resultant $\text{Re}(\epsilon)$ and $\text{Im}(\epsilon)$ values as a function of frequency. Thus, the DFT results presented in Fig. 3a in the main manuscript correspond to the behavior of a polycrystalline material with randomly oriented crystallites, as found in a pressed powder pellet in our experiments. The position of the peaks between 1000-2000 cm^{-1} has been scaled by applying a factor of 0.98, but not the height of the peaks. This scaling factor was implemented so as to empirically compensate for the well-known overestimation in the computed harmonic frequencies, with respect to the fundamental frequencies determined from experiments.

12 References

1. Lucarini, V.; Saarinen, J. J.; Peiponen, K. E.; Vartiainen, E. M. *Kramers-Kronig Relations in Optical Materials Research*. Springer: 2005.
2. Pike_Technologies. *Installation and User Guide - VeeMAX II variable angle specular reflectance accessory*. PIKE Technologies, Inc.: 2012.
3. Fox, M. *Optical Properties of Solids*. Oxford University Press Oxford; 2010.
4. Anderson, J. C. *Dielectrics*. Chapman and Hall Ltd.: London; 1964.
5. Chung, D. L. *Functional Materials: Electrical, Dielectric, Electromagnetic, Optical and Magnetic Applications* World Scientific Publishing Co Pte Ltd: Singapore; 2010.
6. Stassen, I.; Burtch, N.; Talin, A.; Falcaro, P.; Allendorf, M.; Ameloot, R. An updated roadmap for the integration of metal-organic frameworks with electronic devices and chemical sensors. *Chem. Soc. Rev.* **2017**, *46*, 3185-3241.
7. Chalmers, J. M.; Griffiths, P. R. *Handbook of Vibrational Spectroscopy*. Wiley: 2002.
8. Dovesi, R.; Orlando, R.; Erba, A.; Zicovich-Wilson, C. M.; Civalleri, B.; Casassa, S.; Maschio, L.; Ferrabone, M.; De La Pierre, M.; D'Arco, P.; Noel, Y.; Causa, M.; Rerat, M.; Kirtman, B. CRYSTAL14: A Program for the Ab Initio Investigation of Crystalline Solids. *Int. J. Quantum Chem.* **2014**, *114*, 1287-1317.
9. Grimme, S.; Antony, J.; Ehrlich, S.; Krieg, H. A consistent and accurate ab initio parametrization of density functional dispersion correction (DFT-D) for the 94 elements H-Pu. *J. Chem. Phys.* **2010**, *132*.
10. Schäfer, A.; Huber, C.; Ahlrichs, R. Fully optimized contracted Gaussian basis sets of triple zeta valence quality for atoms Li to Kr. *J. Chem. Phys.* **1994**, *100*, 5829-5835.
11. Walker, A. M.; Civalleri, B.; Slater, B.; Mellot-Draznieks, C.; Cora, F.; Zicovich-Wilson, C. M.; Roman-Perez, G.; Soler, J. M.; Gale, J. D. Flexibility in a metal-organic framework material controlled by weak dispersion forces: the bistability of MIL-53(Al). *Angew Chem Int Ed Engl* **2010**, *49*, 7501-3.
12. De la Pierre, M.; Carteret, C.; Orlando, R.; Dovesi, R. Use of ab initio methods for the interpretation of the experimental IR reflectance spectra of crystalline compounds. *J. Comput. Chem.* **2013**, *34*, 1476-1485.